Earthquake Damage Detection in Urban Areas Using Curvilinear Features

Peter T. B. Brett, *Student Member, IEEE*, and Raffaella Guida, *Member, IEEE*

***Abstract*—Bright curvilinear features arising from the geometry of man-made structures are characteristic of synthetic aperture radar (SAR) images of urban areas, particularly due to double-reflection mechanisms. An approach to urban earthquake damage detection using double-reflection line amplitude change in single-look images has been established in previous literature. Based on this method, this paper introduces an automated tool for fast, unsupervised damage detection in urban areas. Ridge-based curvilinear features are extracted from a preevent SAR image, and double-reflection candidates are selected using prior probability distributions derived from a simple geometrical building model. The candidate features are then used with the ratio of a pair of single preevent and postevent SAR single-look amplitude images to estimate damage levels. The algorithm is very efficient, with overall computational complexity of $O(N \log k)$ for an N-pixel image containing features of mean length k. The technique is demonstrated using COSMO-SkyMed data covering L'Aquila, Italy, and Port-au-Prince, Haiti.**

***Index Terms*—Earthquake damage detection, feature extraction, multitemporal synthetic aperture radar (SAR), urban areas.**

I. Introduction

In RECENT years, major earthquakes have struck cities in countries around the globe: China in 2009, Haiti in 2010, Japan in 2011, and Italy in 2009 and 2012. In the case of the magnitude-7 Haiti 2010 earthquake, the Haitian government reported an estimated 230 000 deaths, 300 000 injured, and approximately 1.3 million people displaced both from and within the Port-au-Prince area [1]; the economic damage was estimated to be between $8 billion and $14 billion [2].

When an earthquake strikes, prompt and effective action by disaster response agencies is necessary to minimize loss of life, particularly when considering the survival rate for trapped victims or rescued persons without medical treatment, and the likelihood of secondary disasters, e.g., due to aftershocks or fires [3]. To quickly and accurately organize a response, up-to-date data on affected areas must be made available to response coordinators.

Satellite remote sensing with synthetic aperture radar (SAR) has many benefits for postdisaster data-gathering. Orbital platforms are immune to disruption by terrestrial natural disasters, and unlike optical sensors, SAR is able to penetrate smoke, cloud, and precipitation. The work done under the International Charter on "Space and Major Disasters" [4] and by organizations such as the Operational Satellite Applications Programme of the United Nations Institute for Training and Research (UNOSAT) [5] has enabled the acquisition and distribution of SAR data covering seismic disasters.

In recent years, very high resolution satellite SAR platforms with the ability to resolve meter-scale features have become available, such as COSMO-SkyMed and TerraSAR-X. These have enabled a variety of approaches to urban damage assessment and mapping using multitemporal SAR data, going beyond the well-established use of interferometric SAR to estimate displacement caused by earthquakes [6].

Methods for SAR change detection can broadly be divided into two categories: coherent change detection utilizing phase information (discussed in [7]), and amplitude change detection. At shorter wavelengths, coherence over natural cover cannot be assured even with very short repetition times. Amplitude-based change detection methods are therefore more appealing for seismic disaster monitoring applications, since it is not currently feasible to carry out continual acquisitions covering every area that could possibly be affected by an earthquake.

In recent literature, several interesting approaches to multitemporal amplitude-based urban change detection have been proposed. One approach is to use a difference measure between various different image representations, such as wavelet and curvelet transforms; one stated benefit of curvelets is their strong response to linear features, such as the bright lines caused by double-reflection mechanisms, which is a characteristic of man-made structures [8]. In [9] and [10], the linear features are used to confirm changes detected using a pixel-based approach. By contrast, some approaches to urban damage detection do not consider linear features at all. For example, some information-theoretic methods have been introduced [11], and another promising approach using textural homogeneity even allows the estimation of damage levels using only a single postevent image [12], [13].

In [14] and [15], an approach to damage detection and estimation was introduced, which uses inverse methods to take direct advantage of structures' double-reflection lines. It follows from the closed-form expressions derived in [16] that the radar cross section β^0 of a double-reflection line can be written as [17]

$$\beta^0 = h \cdot f(\boldsymbol{p}) \tag{1}$$

where $\boldsymbol{p}$ is a vector of scene and radar parameters, and h denotes the building height. Assuming $\boldsymbol{p}$ remains constant between

Manuscript received June 22, 2012; revised April 17, 2013; accepted May 24, 2013. Date of publication July 22, 2013; date of current version August 30, 2013. This work was supported by the Engineering and Physical Sciences Research Council under Grants EP/50404X and EP/P503892.

The authors are with the Surrey Space Center, University of Surrey, Surrey GU2 7XH, U.K. (e-mail: p.brett@surrey.ac.uk; r.guida@surrey.ac.uk).

Color versions of one or more of the figures in this paper are available online at http://ieeexplore.ieee.org.

Digital Object Identifier 10.1109/TGRS.2013.2271564

successive acquisitions, the work in [15] describes a method for detecting damage to buildings by detecting changes to their heights using double-reflection lines. In that paper, a damage quotient $0 \leq d \leq 1$ was defined, i.e.,

$$d = \frac{h_1 - h_2}{h_1} = \left(1 - c_r \cdot \frac{\hat{\beta}_2^0}{\hat{\beta}_1^0}\right) \tag{2}$$

where $\hat{\beta}^0$ is the radar cross-sectional estimate for the double-reflection line, and subscripts 1 and 2 denote the preevent and postevent values, respectively. c_r is a calibration coefficient that corrects for differences in attenuation, background noise, and other constant common terms. This d quotient has some shortcomings. There are several classes of earthquake damage that will not be reflected in a gross change in building height (e.g., collapse of internal floors), and it clearly cannot be applied where adjacent buildings or vegetation prevent a double reflection from appearing. It does, however, have some good potential for detecting catastrophic damage where total collapse or the collapse of one or more exterior walls of a building has occurred.

Unfortunately, the results shown in [14] and [15] were based on a manual approach to identifying double-reflection points in the image, which made it impractical to use in an urgent disaster response context.

To address this problem, a way of automating some steps of this damage detection by using ridge detection was outlined in [18], and this paper takes the concept further to present a fully automated tool for the detection of localized damage to buildings in urban areas. The design of the tool is driven by practical goals: 1) high speed, using algorithms with low computational complexity and high scalability to modern multiprocessor computer hardware; 2) flexibility, requiring little or no training or adaptation to apply it to a new target area; and 3) coverage, keeping the number of target areas that the tool can be used on as high as possible by only requiring one recent archive preevent SAR image and one matching postevent SAR image rather than a more extended historical time series.

In Section II, the structure of the tool is described, along with the models and algorithms used. In Section III, the results of applying the tool to data from COSMO-SkyMed covering the 2010 Haiti earthquake are presented, along with some discussion of the tool's effectiveness.

II. Methods

An overview of the process used by the damage detection tool is shown in Fig. 1. The inputs used for damage detection are very high resolution spotlight-mode single-look SAR amplitude images (e.g., the TerraSAR-X SLC or COSMO-SkyMed SSC products). Two images of the target area are used: a library image from a recent acquisition before the event (the *preevent image* X_1), and an image acquired as soon as possible after the event (the *postevent image* X_2). It is assumed that the acquisitions are made with as similar radar and view parameters as possible and that X_2 is coregistered with X_1.

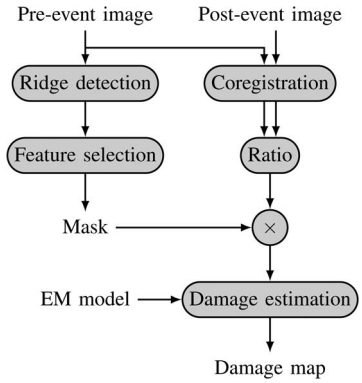

Fig. 1. Flowchart overview of damage detection algorithm operations and data flow.

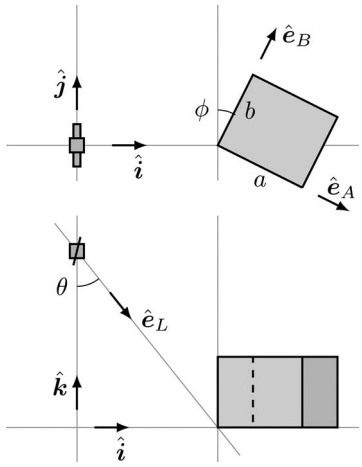

Fig. 2. Geometry of isolated building scene with distant SAR sensor from above (top) and from the side (bottom), showing unit vectors and angles.

There are two main steps to the damage detection process:

1) creation of a *pixel mask* from X_1, which isolates features of interest in the target area, and involves the extraction of curvilinear features using a ridge detector followed by a classification step to select features of interest;
2) Use of the mask and the pre/postratio image X_1/X_2 to identify locations where features of interest have changed, and to estimate damage extent.

A. Double-Reflection Lines and Building Model

The scene model consists of an isolated building with a rectangular footprint of dimensions $a \times b$, $a > 0$, $b > 0$, and smooth vertical walls of height h, surrounded by a level terrain modeled as a generic random rough level surface. In the coordinate system x, y, z, the building lies above the plane $z = 0$, i.e., oriented at an angle $0 \leq \phi \leq \pi/2$ to the y-axis. A SAR observation is made at a look angle $0 < \theta < \pi/2$ by a distant sensor traveling parallel to the y-axis. It is useful to define some unit vectors: $\hat{\boldsymbol{i}}$, $\hat{\boldsymbol{j}}$, $\hat{\boldsymbol{k}}$ along the x-axis, y-axis, and z-axis, respectively; $\hat{\boldsymbol{e}}_L$ along the look axis, and $\hat{\boldsymbol{e}}_A$ and $\hat{\boldsymbol{e}}_B$ parallel to the building walls. This configuration is illustrated in Fig. 2.

Because the dihedral between the smooth walls of the building and the ground forms a corner reflector, double scattering

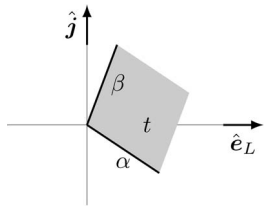

Fig. 3. Geometry of SAR slant range–azimuth image of a bright line in isolated building scene (black) and projected building footprint (gray).

contributions between the walls and the ground all appear at a slant range equal to that of the dihedral's intersection, and the superposition of all the contributions appears as a bright line in the SAR amplitude image. A detailed discussion of this mechanism appears in [16].

The shape of the bright line expected from the model scene is shown schematically in Fig. 3, along with the footprint of the building as projected into the image plane. Note that foreshortening due to the projection means that the building footprint no longer necessarily appears as a rectangle but as a parallelogram.

Let λ_x be the slant range pixel size and λ_y be the azimuth pixel size in the image, both in units of pixels $\cdot$ m^{-1}. Then, some synoptic parameters of the bright line are as follows:

$$t = \lambda_x \sin\theta \cdot \lambda_y \cdot ab \tag{3}$$

$$l = a \left\| \begin{matrix} \lambda_x \sin\theta \sin\phi \\ \lambda_y \cos\phi \end{matrix} \right\| + b \left\| \begin{matrix} \lambda_x \sin\theta \cos\phi \\ \lambda_y \sin\phi \end{matrix} \right\| \tag{4}$$

$$r_e = \left\| \begin{matrix} \lambda_x \sin\theta(b\cos\phi - a\sin\phi) \\ \lambda_y (b\sin\phi + a\cos\phi) \end{matrix} \right\| \tag{5}$$

where $\|\boldsymbol{x}\|$ denotes the l^2-norm, t is the *projected footprint area* (i.e., the area of the enclosed parallelogram), and l and r_e are the total length and *end-to-end distance* of the projected double-reflection line, respectively. Clearly, t is the most attractive classification parameter as it is independent of the unknown building orientation ϕ. However, note also that, if the image is scaled such that $\lambda_y = \lambda_x \sin\theta$, then much simpler relations apply, both of which are independent of ϕ, i.e.,

$$t = \lambda_y^2 ab \tag{6}$$

$$l = \lambda_y (a + b). \tag{7}$$

Let the random variables $A = a$ and $B = b$ correspond to the dimensions of the building, with a joint prior probability density function (pdf) $f_{A,B}(a, b)$. Then, for the case where $\lambda_y \neq \lambda_x \sin\theta$, the pdf of $T = t$, where $c_t = \lambda_x \lambda_y \sin\theta$, is the product distribution

$$f_T(t) = \int_{-\infty}^{\infty} \frac{1}{c_t u} f_{A,B}\left(\frac{t}{c_t u}, u\right) du. \tag{8}$$

For the case where $\lambda_y = \lambda_x \sin\theta$, and including the line length $L = l$, the mapping $(A, B) \mapsto (T, L)$ is bijective and differentiable; therefore, the pdf of the joint distribution of T and L is found by the change of variables as follows:

$$f_{T,L}(t, l) = f_{A,B}(a, b) \frac{2}{\lambda_y \sqrt{l^2 - 4t}} I(l^2 > 4t) \tag{9}$$

where $I(\mathfrak{A})$ denotes the Iverson bracket (1 if $\mathfrak{A}$ holds, 0 if otherwise).

Suppose that it is assumed that the lengths of the sides of the building are independent and identically distributed (i.i.d.). This enables A, $B \sim \Gamma(k, m)$ to be chosen as a model for wall length, with three advantages: 1) it is continuously supported on $[0, \infty]$ as required; 2) the Gamma pdf has several other commonly encountered single-sided continuous distributions as special cases; and 3) both (8) and (9) then conveniently take analytic forms, i.e.,

$$f_T(t|k, m) = \frac{2\left(\frac{t}{c_t m^2}\right)^k K_0\left(2\sqrt{\frac{t}{c_t m^2}}\right)}{t\Gamma^2(k)} I(t > 0) \tag{10}$$

where $K_\alpha(x)$ is the modified Bessel function of the second kind, and

$$f_{T,L}(t, l|k, m) = \frac{2\left(\frac{t}{\lambda_y^2}\right)^{k-1} \exp\left(-\frac{l}{m\lambda_y}\right)}{\Gamma^2(k) m^{2k} \cdot \lambda_y \sqrt{l^2 - 4t}} \times I(t > 0, l > 0, l^2 > 4t). \tag{11}$$

These pdfs are used as the basis for the feature selection process described later in Section II-C.

B. Single-Scale Ridge Detection

Since the intention is to make use of the bright lines caused by double reflections, a method for extracting them from single-look images is required. The approach chosen was to use a *ridge detector* to extract the lines as *curvilinear features*. The form that these lines take matches the *height definition* for ridges in an image [19], and based on this definition, the work in [20] describes a scale-space approach to ridge detection. A brief summary of this method follows.

The *scale-space representation* $L : \mathbb{R}^2 \times \mathbb{R}_+ \to \mathbb{R}$ of the image f is defined by $L(\boldsymbol{r}; \sigma^2) = g(\boldsymbol{r}; \sigma^2) * f$, where the scale parameter σ^2 is the variance of the Gaussian kernel $g : \mathbb{R}^2 \times \mathbb{R}_+ \to \mathbb{R}$. The *scale-space derivatives* are defined by $L_{x^\alpha y^\beta}(\boldsymbol{r}; \sigma^2) = \partial_{x^\alpha y^\beta} L(\boldsymbol{r}; \sigma^2)$, where (α, β) denotes the order of differentiation. At any image point $\boldsymbol{r}$, the eigenvalues k_1 and k_2 and eigenvectors $\boldsymbol{\nu}_1$ and $\boldsymbol{\nu}_2$ of the negated Hessian matrix W are found, where W is formed from the second-order scale-space derivatives, i.e.,

$$W(\boldsymbol{r}; t) = -\begin{bmatrix} L_{xx}(\boldsymbol{r}; t) & L_{xy}(\boldsymbol{r}; t) \\ L_{xy}(\boldsymbol{r}; t) & L_{yy}(\boldsymbol{r}; t) \end{bmatrix} \tag{12}$$

and $|k_1| \geq |k_2|$. A (p, q) coordinate system local to $\boldsymbol{r}$ is defined, which is aligned with $\boldsymbol{\nu}_1$ and $\boldsymbol{\nu}_2$, and $\boldsymbol{r}$ is then a bright ridge point of scale σ^2 if

$$L_{pp}(\boldsymbol{r}_0; \sigma^2) < 0 \quad \text{and} \quad L_p(\boldsymbol{r}; \sigma^2) = 0. \tag{13}$$

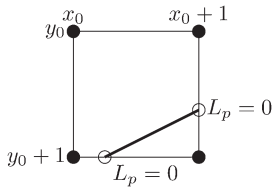

Fig. 4. Each square of four adjacent pixels may contain a single linear ridge segment, formed by joining interpolated points of $L_p = 0$ for which $L_{pp} < 0$.

Ridge points are found by interpolating for zero crossings of L_p along the vertical and horizontal edges joining adjacent pixels and by testing the sign of the interpolated value of L_{pp} at each zero crossing found. If the square formed by four adjacent pixels has exactly two ridge points on its perimeter, a *ridge segment* is formed by joining them with a straight line. This is illustrated in Fig. 4.

This ridge detection algorithm is very suitable for a symmetric multiprocessing implementation because all of the computationally intensive steps can be implemented using *wait-free* approaches. A wait-free implementation of a concurrent data object is one that guarantees that any process can complete any operation in a finite number of steps, regardless of the execution speeds of the other processes [21]. When wait-free methods are used, multiple processes can read and write to the same shared memory without locking, avoiding any execution time being wasted, copying memory between processes, or waiting for locks to be released.

If separable finite-impulse-response approximations for the Gaussian kernel g and the derivative operator ∂ are used (e.g., the discrete scale-space formulation proposed in [22]), the generation of the scale-space representation and scale-space derivatives can be carried out in parallel by dividing the individual linear convolutions between multiple processors. This also applies to the generation of the metrics L_{pp} and L_p, and to the interpolation for and detection of ridge points. For an n-pixel image, the complexity of the ridge detection is $O(\sigma^2 n)$ for the scale-space generation and $O(n)$ for ridge point detection.

A method is described in [20] for multiscale ridge detection, wherein a normalized *ridge strength metric* $\mathcal{R}_{\mathrm{norm}}L$ is used to select the optimal scale for a ridge point. Unfortunately, for a typical SAR image (with a size on the order of 10^8 pixels), prohibitively large amounts of memory are required for the creation of the scale-space and ridge metrics. Instead, the approach presented in this paper is based on carrying out ridge extraction at a single empirically determined characteristic scale σ_c^2, which is subjected to the requirement that

$$\sigma_c^2 \geq \frac{w^2}{12} \tag{14}$$

where w is the maximum line width to be detected [23].

The ridge segments located using the ridge detector are next linked to form longer *ridge lines*. Since these lines may span the image, this is a highly nonlocal problem, and simple task-division approaches to parallel computation (as used for the ridge segment detection described in the previous section) cannot be used.

The ridge segment detection process ensures that any given ridge segment can be only a member of a single line; thus, the lines $\Lambda = \{l_i\}$ can be considered to be disjoint sets of segments s_i, i.e.,

$$l_i \cap l_j = \oslash \qquad \forall j \neq i. \tag{15}$$

Initially, a single-element set is created for each ridge segment. Adjacent segments are then tested pairwise for connectedness. If they are connected, the sets they belong to are merged in a set-union operation. The disjoint–merge algorithm used is described in [24] and has the advantages for this application, i.e., it is wait-free with the concomitant benefits described earlier in this section, the primitive atomic "compare-and-swap" operation that it relies on for synchronization is available on most modern CPU architectures, and merges may be carried out in any order to obtain the same result. This algorithm is also highly efficient for an image containing M line segments in lines of mean length $\tilde{N}$, which complexity is approximately $O(M \log \tilde{N})$.

Once the line merging has been completed, there exists exactly one disjoint set l_i for each line in the image. Each line's set is then transformed in place to a more convenient linked-list structure, and loops are detected and removed. This step is once again easy to divide between multiple processes.

C. Geometry-Based Feature Selection

For each N-point feature $C = \{\boldsymbol{r}_1, \boldsymbol{r}_2, \ldots, \boldsymbol{r}_N\}$ extracted by the ridge detection process described in Section II-B, it must be determined how well C conforms to the expected geometry of a building's double-reflection line. To do so based on the model described in Section II-A and using (10) or (11), the synoptic parameters t and l are estimated as follows.

First, C is translated to the origin such that $\boldsymbol{r}_0 = \mathbf{0}$. The length is then trivially given by

$$\tilde{l} = \sum_{i=1}^{N-1} \|\boldsymbol{r}_{i+1} - \boldsymbol{r}_i\|. \tag{16}$$

The area contained by C was estimated from the end-to-end distance r_e and the radius of gyration r_g^2 around the end-to-end axis

$$\tilde{r}_e = \|\boldsymbol{r}_N\| \tag{17}$$

$$\tilde{r}_g^2 = \frac{1}{N\tilde{r}_e^2} \sum_{i=1}^{N-1} \|\boldsymbol{r}_i \times \boldsymbol{r}_N\|^2. \tag{18}$$

To relate this to projected footprint area, consider the canonical double-reflection line shape as the triangle shown in Fig. 5. Let it be composed of N discrete points $\boldsymbol{r}_i$ at perpendicular distance u_i from the end-to-end-axis. Let the sides, of length α and β, respectively, contain N_A and N_B equally spaced points. Then, (18) can be rewritten as

$$r_g^2 = \frac{1}{N} \sum_{i=1}^{N} u_i^2 \qquad u_i = \begin{cases} \frac{i}{N_A} d & i \leq N_A \\ \frac{N-i}{N_B} d & i > N_A. \end{cases} \tag{19}$$

In the limit of large N_A and N_B, this becomes

$$\lim_{N_A, N_B \to \infty} r_g^2 = \frac{d^2}{3}. \tag{20}$$

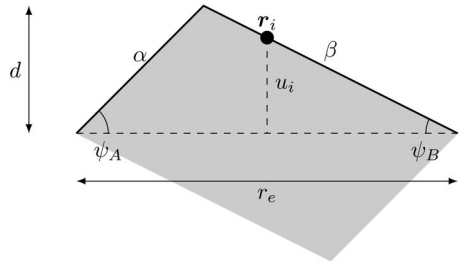

Fig. 5. Double-reflection line with projected footprint area $t = d \cdot r_e$ and points $\boldsymbol{r}_i$ spaced along the area.

The projected footprint area $t = d \cdot r_e$ can be therefore estimated from the curvilinear feature measures r_e and r_g according to the relation

$$\tilde{t} = \tilde{r}_e \cdot \sqrt{3\tilde{r}_g^2}. \tag{21}$$

These statistics are then used to classify each feature, using a simple *likelihood threshold decision rule,* i.e.,

$$\log p(C|\boldsymbol{\vartheta}) \underset{\bar{\mathcal{B}}}{\overset{\mathcal{B}}{\gtrless}} \tau \tag{22}$$

where $\mathcal{B}$ denotes classification as a feature of interest, τ is the likelihood threshold, and $\boldsymbol{\vartheta}$ is the parameter vector for the chosen model [either (10) or (11)].

The features matching $\mathcal{B}$ are used as the input for the damage detection and estimation step.

D. Change Detection and Estimation

The amplitude ratio image $R = X_1/X_2$ is used to calculate a severity-of-change measure $d(\boldsymbol{r})$ at a point $\boldsymbol{r}$, which is based on (2) with c_r approximated by the global mean of R

$$\tilde{d}(\boldsymbol{r}) = \left(1 - \frac{\langle R \rangle}{R(\boldsymbol{r})}\right). \tag{23}$$

The tool described in this paper locates seismic damage by creating a mask image that includes all pixels of R intersected by the features of interest selected in Section II-C. It then uses (23) as a severity-of-change metric, applying it to each unmasked pixel in R to generate the output image showing detected change locations and change strength.

As in Section I, there are two principal drawbacks to applying this approach to seismic damage estimation. First, damage can be only obviously detected for buildings where a suitable double-reflection line is present in the preevent image X_1. If no suitable line is visible (due, for example, to adjacent buildings or vegetation blocking the wall–ground corner reflector), then even very extensive damage cannot be detected. Unfortunately, this is a fundamental limitation of the approach and can be only addressed by, for example, fusion with other seismic damage detection approaches. Second, only very severe structural damage can be reliably detected in this way, involving the total collapse of a building or of at least one of its walls.

TABLE I
RIDGE DETECTION PERFORMANCE

Image size (px)	1024×1024	5778×6092
1 core, elapsed (s)	2.82	61.0
4 cores, elapsed (s)	0.773	20.3
1 core, relative (px^{-1})	1	0.644
4 cores, relative (px^{-1})	0.274	0.214

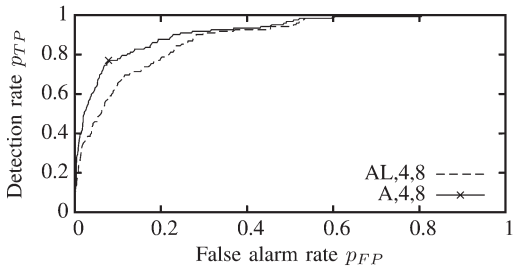

Fig. 6. Empirical ROC curves for likelihood threshold detection using area (A) and area–length (AL) models and a building size prior $A \sim \Gamma(4, 10)$, derived using manual classification of selected sites in L'Aquila, Italy. The maximum discrimination point for the A model is marked.

III. RESULTS

Two sets of experiments were carried out: tests of the performance of the feature selection approach, and tests using selected features for seismic damage detection.

For the purposes of this paper, a prior $A \sim \Gamma(4, 10)$ was empirically chosen as models for medium-size buildings of mean side length of 40 m, and curvilinear features were extracted at a scale $\sigma_c^2 = 8$.

A. Ridge Detection Performance Results

Some experiments were carried out to verify the computational scalability of the ridge detector described in Section II-B. The tests were carried using a single-look SAR amplitude image of L'Aquila, Italy, acquired by the COSMO-SkyMed constellation on March 22, 2009 with a look angle of 20°. Two sections of the image were used: a smaller segment with 1024×1024 pixels, and a larger segment with 5778×6092 pixels. Ridge extraction was carried out first using a single core of 2.67-GHz Intel Core i5 CPU, and then again using all four cores. Each test was repeated ten times, and the mean elapsed time was measured.

Table I shows the elapsed time and a relative per-pixel processing time for each test. The single-core results suggest that the ridge detection scales slightly better than $O(N)$ for N pixels. With smaller images, proportionately more of the run time is committed to fixed-cost or particularly costly tasks (e.g., memory allocation). For the smaller image, four-core results show approximately $1/k$ run time for k cores, as expected. The four-core task for the larger image has smaller speed-up than on a single core possibly because, for the 4-core tests, the speed was limited by memory bandwidth rather than by CPU time. The scalability objectives for the algorithm design were successfully achieved.

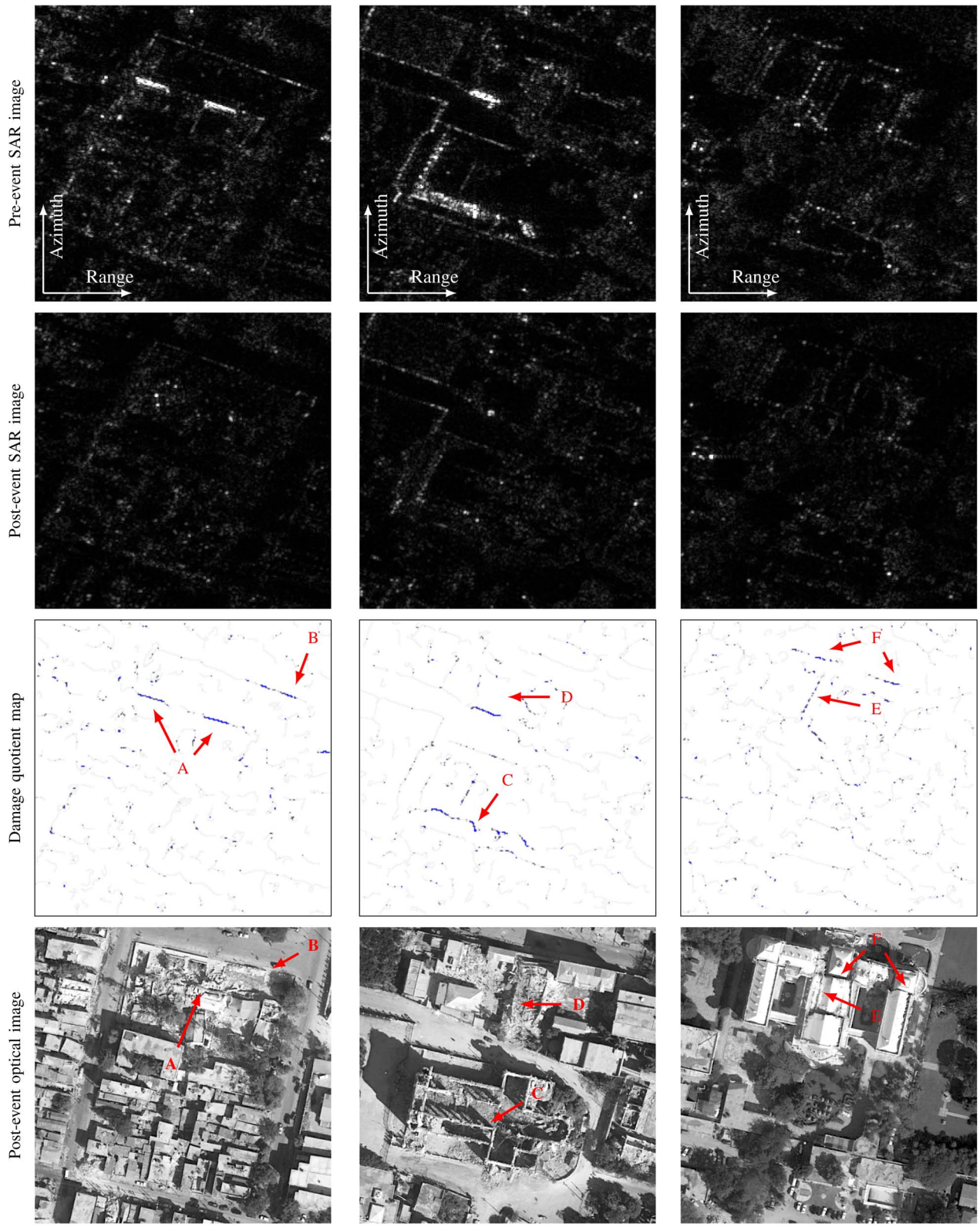

(a) Supreme Court. (b) Cathedral. (c) National Palace.

Fig. 7. Damage detection results from selected sites in Port-au-Prince, Haiti. Damage quotient gradient from white to gray for $d = 0.75$ to blue at $d = 1$. Optical images GeoEye 2010. COSMO-SkyMed product Agenzia Spaziale Italiana 2009–2010. All rights reserved. (a) Supreme Court. (b) Cathedral. (c) National Palace.

B. Feature Selection Results

The feature selection was tested using the same SAR image of L'Aquila, Italy. The product was processed with azimuth and ground range resolutions of 0.85 m, giving $\lambda_y = 1.18$ px $\cdot$ m^{-1} and $c_t = 1.38$ px$^2 \cdot$ m^{-2}. Three 256 $\times$ 256-pixel image segments were chosen from the image, and the curvilinear

features extracted from them were manually classified. These results were compared with the results of feature selection to generate receiver operating characteristic (ROC) curves, shown in Fig. 6. From these ROC curves, it was evident that better detection performance was achieved using the area model (10) than with the area–length model (11). A possible reason for this may have been that the more selective model is also more sensitive to choice of building size prior distribution.

A suitable likelihood threshold for classification was set by choosing the value of τ that gave maximum detection discrimination, i.e.,

$$\tau_{D\max} = \arg\max_{\tau}(p_{\mathrm{TP}} - p_{\mathrm{FP}}). \tag{24}$$

This gave a threshold for the area model of $\tau = -12.9$, with accuracy of 91.7%, a miss rate of 23%, and a false alarm rate of 7.8%. This operating point is marked in Fig. 6.

C. Damage Detection Results

The tool as a whole was tested by applying it to a pair of single-look SAR amplitude images of Port-au-Prince, Haiti, acquired by the COSMO-SkyMed constellation. The preevent image X_1 was acquired on December 12, 2009, and the postevent image X_2 on January 21, 2010. Both images were acquired in high-resolution spotlight mode with a look angle of $\theta = 38.2^\circ$, and the products were processed with azimuth and *ground* range resolutions of 1 m, giving $c_t = 1\ \mathrm{px}^2 \cdot \mathrm{m}^{-2}$. The area model (10) was used to select curvilinear features, with a likelihood threshold $\tau = 5 \times 10^{-6}$. The underlying assumptions that (23) depends on are valid for this image pair, due to the close similarity of the acquisition parameters.

Three 256×256 pixel image segments of the coregistered image pair were selected for testing, centering on major buildings in central Port-au-Prince that were known to have been heavily damaged, i.e., the Supreme Court, a cathedral, and the National Palace. The results of applying the tool to these image segments are shown in Fig. 7.

Fig. 7(a) shows the results of applying the tool to the segment covering the Haiti Supreme Court building, which was completely destroyed by the earthquake. The main building provided two strong curvilinear feature responses in the preevent image, which were removed entirely by the destruction of the building. These are labeled A in the figure. In addition to the main building, the postevent optical image shows that a section of the site's peripheral wall is missing. This smaller change is also successfully detected, which is labeled B in the figure.

The cathedral and nearby buildings are shown in Fig. 7(b). The cathedral roof collapsed during the earthquake, but the walls of the cathedral remain mostly intact. This, along with the tool's failure to locate suitable curvilinear features near the cathedral, meant that the tool identified only limited damage here (labeled C). By contrast, the tool detects a very strong ($90\%+$) degree of damage to the north of the cathedral, which is labeled D, near a building that can clearly be seen to be collapsed in the optical image.

The third segment, covering the National Palace, is shown in Fig. 7(c). This structure was damaged by the earthquake, but the level of damage was relatively minor. The roof of the central wing of the palace subsided (E) and the central and eastern towers of the palace also partially collapsed (F). All these effects were detected successfully by the tool. In this case, note that the tool is reporting $75\%+$ degree of damage, although the total damage to the structure is much less than that. This occurred because, despite being only a small element of the overall building, the dihedral that caused the bright line used by the tool for damage estimation was very heavily damaged in proportion to its size.

IV. Conclusion

This paper has introduced a proof-of-concept tool for detecting earthquake-damaged structures in urban areas, based on the detection of changes to selected curvilinear features. The tool is designed to provide data as promptly as possible in the aftermath of an earthquake, due to the selection of algorithms with low computation complexity; the avoidance of manual/supervised steps where possible; and the use of a minimal number of observations. It does, however, require two images acquired with as similar acquisition parameters as possible in order to be applicable; on the other hand, this requirement can often be easily satisfied.

Applying the tool to COSMO-SkyMed SAR images to detect damage in Port-au-Prince due to the 2010 Haiti earthquake demonstrated the ability to locate serious damage to urban structures, in line with damage estimates made from postearthquake optical images. A number of drawbacks are also evident from the results, including the problem of false alarms from large changes to small features, and the inability to detect damage to buildings that do not have backscattering patterns with curvilinear features that match the building model used.

The approach has a good potential for further development and investigation, including the possibility of introducing alternative geometry models, and improving performance of the technique by combining it with other change detection algorithm methods. For example, combining the technique with the texture-based approach described in [12] and [13] would allow damage to be detected in a city block without suitable double-reflection lines while still providing specific per-building damage detection where possible. In addition, further work should, if possible, include a more detailed quantitative assessment of the degree of correlation between the severity of change detected and ground-truth damage maps.

Nevertheless, in its current state, the tool described in this paper provides a capable method for identifying and assessing particular critically damaged structures in an urban area in the wake of an earthquake.

V. Code Availability

The GPL-licensed source code is available for the ridge detection tools described in Section II-B [25], for the classification tools described in Section II-C [26], and for the change estimation and visualization tool described in Section II-D [27].

ACKNOWLEDGMENT

The authors would like to thank Agenzia Spaziale Italiana for providing the COSMO-SkyMed SAR images used in this study, and B. Donlan for the advice on the use of disjoint sets.

REFERENCES

[1] R. Margesson and M. Taft-Morales, Haiti earthquake: Crisis and response, Congr. Res. Service, Library of Congr., Washington, DC, USA. [Online]. Available: http://www.dtic.mil/dtic/tr/fulltext/u2/a516429.pdf
[2] E. Cavallo, A. Powell, and O. Becerra, "Estimating the direct economic damages of the earthquake in Haiti," *Econ. J.*, vol. 120, no. 546, pp. F298–F312, Aug. 2010.
[3] F. Fiedrich, F. Gehbauer, and U. Rickers, "Optimized resource allocation for emergency response after earthquake disasters," *Safety Sci.*, vol. 35, no. 1, pp. 41–57, Jun. 2000.
[4] 2012. [Online]. Available: http://www.disasterscharter.org/
[5] 2012. [Online]. Available: http://www.unitar.org/unosat/
[6] P. Rosen, S. Hensley, I. Joughin, F. Li, S. Madsen, E. Rodriguez, and R. Goldstein, "Synthetic aperture radar interferometry," *Proc. IEEE*, vol. 88, no. 3, pp. 333–382, Mar. 2000.
[7] P. Wright, T. Macklin, C. Willis, and T. Rye, "Coherent change detection with SAR," in *Proc. Eur. Radar Conf.*, Oct. 2005, pp. 17–20.
[8] A. Schmitt, A. Wendleder, B. Wessel, and A. Roth, "Comparison of alternative image representations in the context of SAR change detection," in *Proc. IEEE IGARSS*, Jul. 2010, pp. 284–287.
[9] P. Gamba, F. Dell'Acqua, and G. Lisini, "Change detection of multitemporal SAR data in urban areas combining feature-based and pixel-based techniques," *IEEE Trans. Geosci. Remote Sens.*, vol. 44, no. 10, pp. 2820–2827, Oct. 2006.
[10] P. Gamba, F. Dell'Acqua, and G. Trianni, "Rapid damage detection in the Bam area using multitemporal SAR and exploiting ancillary data," *IEEE Trans. Geosci. Remote Sens.*, vol. 45, no. 6, pp. 1582–1589, Jun. 2007.
[11] S. Cui, M. Datcu, and L. Gueguen, "Information theoretical similarity measure for change detection," in *Proc. Joint Urban Remote Sens. Event*, Munich, Germany, Apr. 2011, pp. 69–72.
[12] F. Dell'Acqua, G. Lisini, and P. Gamba, "Experiences in optical and SAR imagery analysis for damage assessment in the Wuhan, May 2008 earthquake," in *Proc. IEEE IGARSS*, Cape Town, South Africa, Jul. 2009, vol. 4, pp. 37–40.
[13] F. Dell'Acqua, P. Gamba, and D. Polli, "Earthquake damage assessment from post-event VHR radar data: From Sichuan, 2008 to Haiti, 2010," in *Proc. Joint Urban Remote Sens. Event*, Munich, Germany, Apr. 2011, pp. 201–204.
[14] R. Guida, A. Iodice, and D. Riccio, "An application of the deterministic feature extraction approach to COSMO-SkyMed data," in *Proc. 8th Eur. Conf. Synth. Aperture Radar*, Aachen, Germany, Jun. 2010, pp. 1–4.
[15] R. Guida, A. Iodice, and D. Riccio, "Monitoring of collapsed built-up areas with high resolution SAR images," in *Proc. IEEE IGARSS*, Honolulu, HI, USA, Jul. 2010, pp. 2422–2425.
[16] G. Franceschetti, A. Iodice, and D. Riccio, "A canonical problem in electromagnetic backscattering from buildings," *IEEE Trans. Geosci. Remote Sens.*, vol. 40, no. 8, pp. 1787–1801, Aug. 2002.
[17] R. Guida, A. Iodice, and D. Riccio, "Height retrieval of isolated buildings from single high-resolution SAR images," *IEEE Trans. Geosci. Remote Sens.*, vol. 48, no. 7, pp. 2967–2979, Jul. 2010.
[18] R. Guida and P. T. B. Brett, "A SAR image-based tool for prompt and effective earthquake response," in *Proc. Joint Urban Remote Sens. Event*, Munich, Germany, Apr. 2011, pp. 213–216.
[19] D. Eberly, R. Gardner, B. Morse, S. Pizer, and C. Scharlach, "Ridges for image analysis," *J. Math. Imaging Vis.*, vol. 4, no. 4, pp. 353–373, Dec. 1994.
[20] T. Lindeberg, "Edge detection and ridge detection with automatic scale selection," *Int. J. Comput. Vis.*, vol. 30, no. 2, pp. 117–154, Nov. 1998.
[21] M. Herlihy, "Wait-free synchronization," *ACM Trans. Programm. Lang. Syst.*, vol. 13, no. 1, pp. 124–149, Jan. 1999.
[22] J. Lim and H. Stiehl, "A generalized discrete scale-space formulation for 2-D and 3-D signals," in *Proc. Scale Space Methods Comput. Vis.*, 2003, pp. 132–147.
[23] C. Steger, "An unbiased detector of curvilinear structures," *IEEE Trans. Pattern Anal. Mach. Intell.*, vol. 20, no. 2, pp. 113–125, Feb. 1998.
[24] R. J. Anderson and H. Woll, "Wait-free parallel algorithms for the union-find problem," in *Proc. 23rd ACM Symp. Theory Comput.*, New York, NY, USA, 1991, pp. 370–380.
[25] P. T. B. Brett, SSC ridge tools 1.0.1. figshare, Jun. 2013.
[26] P. T. B. Brett, SSC ridge classifiers 1.0. figshare, Jun. 2013.
[27] P. T. B. Brett, SSC urban change detection 1.0. figshare, Jun. 2013.

Peter T. B. Brett (S'12) was born in Berkshire, U.K., on September 9, 1985. He received the B.A. (Hons.) degree and M.Eng. degree (with distinction) in engineering from the University of Cambridge, Cambridge, U.K., in 2009. He is currently working toward the Ph.D. degree at the Surrey Space Center (SSC), University of Surrey, Surrey, U.K., studying remote sensing applications and, in particular, the topic of change detection and urban monitoring with synthetic aperture radar.

From September 2004 to September 2005, he was a Year-in-Industry Student with Sharp Laboratories of Europe Ltd., Oxford, U.K. In 2008, he was a Placement Student with Cambridge Silicon Radio, Cambridge, U.K.

Mr. Brett is a member of the Institute of Engineering and Technology. He received a Doctoral Training Grant from the U.K. Engineering and Physical Sciences Research Council in 2009 for a Ph.D. studentship with SSC.

Raffaella Guida (S'04–M'08) was born in Naples, Italy, on October 24, 1975. She received the Laurea degree (*cum laude*) in telecommunications engineering and the Ph.D. degree in electronic and telecommunications engineering from the University of Naples Federico II, Naples, Italy, in 2003 and 2007, respectively.

In 2006, she was a Guest Scientist with the Department of Photogrammetry and Remote Sensing, Technical University of Munich, Munich, Germany. In 2008, she joined the Surrey Space Center (SSC), University of Surrey, Surrey, U.K., as a Lecturer of satellite remote sensing. She is currently with Remote Sensing Applications Group, SSC. Her main research interests include electromagnetism and microwave remote sensing, particularly in simulation and modeling of synthetic aperture radar signals relevant to natural surfaces and urban scenes, and new remote sensing mission concepts and applications.

Dr. Guida received a two-year research grant from the University of Naples Federico II in 2006, to be spent at the Department of Electronic and Telecommunication Engineering on the topic of electromagnetic field propagation in urban environment.